

# **PAIN AND SUFFERING IN THE NETHERLANDS**



# **PAIN AND SUFFERING IN THE NETHERLANDS**

## **Proefschrift**

ter verkrijging van de graad van doctor  
aan de Technische Universiteit Delft,  
op gezag van de Rector Magnificus Prof. dr. ir. T.H.J.J. van der Hagen,  
voorzitter van het College voor Promoties,  
in het openbaar te verdedigen op dinsdag 1 januari 2022 om 10:00 uur

door

**Ryan LANE**

Master of Science in Physics,  
University of Oregon, Verenigde Staten van Amerika,  
geboren te Carlisle, Verenigde Staten van Amerika.

Dit proefschrift is goedgekeurd door de promotoren.

Samenstelling promotiecommissie:

Rector Magnificus,	voorzitter
Dr. J.P. Hoogenboom,	Technische Universiteit Delft, promotor
Dr. E.C.M. Carroll,	Technische Universiteit Delft, copromotor

*Onafhankelijke leden:*

Prof. dr. A. Jansen	Technische Universiteit Delft
Prof. dr. ir. A.B.C.D. van de Lange-Achternaam	Technische Universiteit Delft
Prof.dr. N. Nescio	Politecnico di Milano, Italië
Prof. dr. ir. J. Doe,	Technische Universiteit Delft, reservelid

*Overige leden:*

Prof. dr. ir. J. de Wit,	Technische Universiteit Delft
Dr. ir. Q. de Zwart,	Technische Universiteit Eindhoven



**Genentech**



*Keywords:* ...

*Printed by:* Johannes Gutenberg

*Front & Back:* Beautiful cover art that captures the entire content of this thesis in a single illustration.

Copyright © 2022 by R. Lane

ISBN 000-00-0000-000-0

An electronic version of this dissertation is available at  
<http://repository.tudelft.nl/>.

# CONTENTS

<b>Summary</b>	<b>vi</b>
<b>1 Introduction</b>	<b>1</b>
1.1 So you want to know how the brain works? . . . . .	1
1.2 Volume electron microscopy . . . . .	2
1.3 Correlative light and electron microscopy . . . . .	2
1.4 Integrated microscopy . . . . .	3
1.5 Integrated correlative array tomography . . . . .	3
<b>2 Integrated array tomography</b>	<b>9</b>
2.1 Introduction . . . . .	10
2.2 Material & methods . . . . .	11
2.2.1 Tissue and sample preparation . . . . .	11
2.2.2 Digital light microscopy . . . . .	11
2.2.3 Integrated microscopy . . . . .	11
2.2.4 Alignment and reconstruction software . . . . .	12
2.3 Results . . . . .	12
2.3.1 Section detection and <i>in-situ</i> navigation . . . . .	12
2.3.2 Targeted correlative acquisition of an individual region of interest . . . . .	14
2.3.3 2D Stitching and correlation. . . . .	14
2.3.4 Correlative 3D reconstruction . . . . .	17
2.3.5 Proof of concept on zebrafish pancreas tissue . . . . .	18
2.4 Discussion . . . . .	20
2.5 Supplementary material. . . . .	23

# SUMMARY

Summary in English. Hello, here is some text without a meaning. This text should show what a printed text will look like at this place. If you read this text, you will get no information. Really? Is there no information? Is there a difference between this text and some nonsense like “Huardest gefburn”? Kjift – not at all! A blind text like this gives you information about the selected font, how the letters are written and an impression of the look. This text should contain all letters of the alphabet and it should be written in of the original language. There is no need for special content, but the length of words should match the language.

A new paragraph with a citation [1]. Let us also add some numbers with units like 100 mg and even a range of units 14–27 kPa. Hello, here is some text without a meaning. This text should show what a printed text will look like at this place. If you read this text, you will get no information. Really? Is there no information? Is there a difference between this text and some nonsense like “Huardest gefburn”? Kjift – not at all! A blind text like this gives you information about the selected font, how the letters are written and an impression of the look. This text should contain all letters of the alphabet and it should be written in of the original language. There is no need for special content, but the length of words should match the language. Could also look at units in math mode like 13.8 N/m. Let’s follow this up with some math [2].

Hello, here is some text without a meaning. This text should show what a printed text will look like at this place. If you read this text, you will get no information. Really? Is there no information? Is there a difference between this text and some nonsense like “Huardest gefburn”? Kjift – not at all! A blind text like this gives you information about the selected font, how the letters are written and an impression of the look. This text should contain all letters of the alphabet and it should be written in of the original language. There is no need for special content, but the length of words should match the language.

$$\bar{x} = \frac{1}{n} \sum_{i=1}^{i=n} x_i = \frac{x_1 + x_2 + \dots + x_n}{n}$$

Hello, here is some text without a meaning. This text should show what a printed text will look like at this place. If you read this text, you will get no information. Really? Is there no information? Is there a difference between this text and some nonsense like “Huardest gefburn”? Kjift – not at all! A blind text like this gives you information about the selected font, how the letters are written and an impression of the look. This text should contain all letters of the alphabet and it should be written in of the original language. There is no need for special content, but the

length of words should match the language.

$$\int_0^{\infty} e^{-\alpha x^2} dx = \frac{1}{2} \sqrt{\int_{-\infty}^{\infty} e^{-\alpha x^2} dx} \int_{-\infty}^{\infty} e^{-\alpha y^2} dy = \frac{1}{2} \sqrt{\frac{\pi}{\alpha}}$$

Hello, here is some text without a meaning. This text should show what a printed text will look like at this place. If you read this text, you will get no information. Really? Is there no information? Is there a difference between this text and some nonsense like “Huardest gefburn”? Kjift – not at all! A blind text like this gives you information about the selected font, how the letters are written and an impression of the look. This text should contain all letters of the alphabet and it should be written in of the original language. There is no need for special content, but the length of words should match the language.

$$\sum_{k=0}^{\infty} a_0 q^k = \lim_{n \rightarrow \infty} \sum_{k=0}^n a_0 q^k = \lim_{n \rightarrow \infty} a_0 \frac{1 - q^{n+1}}{1 - q} = \frac{a_0}{1 - q}$$

Hello, here is some text without a meaning. This text should show what a printed text will look like at this place. If you read this text, you will get no information. Really? Is there no information? Is there a difference between this text and some nonsense like “Huardest gefburn”? Kjift – not at all! A blind text like this gives you information about the selected font, how the letters are written and an impression of the look. This text should contain all letters of the alphabet and it should be written in of the original language. There is no need for special content, but the length of words should match the language.

$$x_{1,2} = \frac{-b \pm \sqrt{b^2 - 4ac}}{2a} = \frac{-p \pm \sqrt{p^2 - 4q}}{2}$$

Hello, here is some text without a meaning. This text should show what a printed text will look like at this place. If you read this text, you will get no information. Really? Is there no information? Is there a difference between this text and some nonsense like “Huardest gefburn”? Kjift – not at all! A blind text like this gives you information about the selected font, how the letters are written and an impression of the look. This text should contain all letters of the alphabet and it should be written in of the original language. There is no need for special content, but the length of words should match the language.

$$\frac{\partial^2 \Phi}{\partial x^2} + \frac{\partial^2 \Phi}{\partial y^2} + \frac{\partial^2 \Phi}{\partial z^2} = \frac{1}{c^2} \frac{\partial^2 \Phi}{\partial t^2}$$

Hello, here is some text without a meaning. This text should show what a printed text will look like at this place. If you read this text, you will get no information. Really? Is there no information? Is there a difference between this text and some nonsense like “Huardest gefburn”? Kjift – not at all! A blind text like this gives you information about the selected font, how the letters are written and an impression of the look. This text should contain all letters of the alphabet and it should be written in of the original language. There is no need for special content, but the length of words should match the language.





# 1

## INTRODUCTION

### 1.1. So you want to know how the brain works?

How a convoluted network of synapses can enable an animal to think and exhibit complex behavior has been a motivating question of neuroscience since the discovery of neurons in the late 19<sup>th</sup> century [1, 2]. Neuronal circuit diagrams, maps delineating the connections between synapses, have shown to be useful tools for better understanding cognitive function and neural architecture [3, 4]. Although several full brain circuit diagrams have been completed (*C. elegans* [5], fruit fly larva [6], tunicate tadpole larva [7], zebrafish larva [8], and adult fruit fly [9]), such “connectomes” are a herculean task given that the resolution required to discern synapses is on the nanometer scale, while the organ as a whole spans millimeters or larger, depending on the organism [10, 11, 12]. Electron microscopy (EM), an imaging technique able to reach magnification scales several orders of magnitude higher than light microscopy by illuminating a specimen with a beam of accelerated electrons, is currently the only imaging method capable of resolving such fine features across such vast spatial extents [3, 9]. The drawback for high-magnification imaging over organ-scale dimensions is, however, the inherently limited throughput, leading to hours or days of acquisition time for a single two-dimensional cross section. Extending acquisitions of biological material to the third dimension has long remained a challenge for EM.

While the brain is perhaps the most prominent, it is certainly not the only example in biology where multi-scale microscopy can assist in mapping connectivity relations crucial to functional performance. Molecular-scale processes taking place within cells or organelles are highly regulated in health, and defects or deviations at the smallest scales can lead to dysfunction or disease at the organ or organism level. Simply put, the big things are made out of lots of little things, and to figure out how the big thing works, you have to look at all the little things. EM is the only technique that can see the littlest things and that might do this over the full size of the big things.

## 1.2. Volume electron microscopy

There are a variety of techniques for three-dimensional imaging of biological specimen via electron microscopy (EM) [13]. Modern volume EM techniques can be divided into two broader methods: array tomography approaches, in which ultrathin serial sections are cut from a block of tissue prior to EM (e.g. serial section scanning EM or transmission EM), and blockface approaches, in which the tissue block is sectioned as it is imaged (e.g. serial blockface or focused ion beam SEM). While both of these approaches have their respective advantages and disadvantages [14, 13], an important distinction is that array tomography allows for re-evaluation of sections whereas the specimen is irrevocably lost in blockface approaches [15].

Despite the success these techniques have had in generating high-quality three-dimensional reconstructions, significant challenges remain. At present, one of the most stringent constraints facing high-resolution ( $< 10$  nm) volume EM is throughput. To scan an entire mouse cortical column, for example, a  $400 \times 400 \times 1000 \mu\text{m}^3$  volume, at 4 nm/px with 30 nm section thickness (the resolution necessary to reliably discern synapses [16, 17]), Briggman and Bock [14] estimated that it would require  $\sim 500$  days of uninterrupted imaging with a single beam. For this reason, it is advantageous to locate regions of interest prior to large-scale EM in order to minimize the imaging volume.

One approach, taken by Hildebrand et al. [8] for whole-brain serial section SEM reconstruction of a larval zebrafish, was to utilize multiple rounds of targeted EM at successively higher levels of magnification. Similar approaches have been taken in other large-scale neural reconstruction endeavors such as partial brain imaging of a mouse visual cortex [11] and full brain imaging of an adult fruit fly [9] where certain synapses were re-imaged at higher resolution. Although these multiscale approaches have been implemented with great success, the need for intermediate analysis of the EM dataset hinders throughput. The selection of sub-regions of interest for subsequent imaging rounds is driven by localization of the biological material of interest, which can only be done after manual or machine-learning-assisted analysis of the preceding EM dataset. While machine-learning techniques have made tremendous progress in reducing human involvement, interpretation and annotation of EM datasets remain a tedious and error-prone practice. These methods are therefore not yet appropriate for selecting sub-regions at higher magnification scales, meaning selection cannot be done either automatically or in real time.

## 1.3. Correlative light and electron microscopy

In addition to low throughput, EM has the additional limitation that it does not contain the protein- and molecular-specific information available from fluorescence microscopy (FM)—unless the proteins are known to be specifically linked to a structural component. This information is not only crucial for understanding biological function but can also be used to guide to regions of interest (ROI) based on molecular expression. Thus, while EM is successful at providing ultrastructural information, it is not always useful for localizing ROIs. Functional fluorescence

microscopy has been employed to identify the biological material of interest, particularly in blockface approaches [18]. However, workflows to retrieve selected regions from the specimen and trim the block to the appropriate size can be both complicated and time-consuming or involve further rounds of multimodal inspection, e.g. with X-ray tomography [19]. Linking between the structural information conveyed by EM and the dynamic, functional data obtained with live-cell FM can furthermore be challenging when EM is performed following FM and the intermediate sample preparation [20].

As the advantages afforded by merging targeted biological information with ultrastructural detail often outweigh the challenges, methods have been developed for combining FM and EM in correlative light and electron microscopy (CLEM). In the past decades, CLEM has evolved from being used by only a few pioneering, specialist labs to a collection of techniques and workflows practiced by a broad group of researchers in structural biology [20, 21]. In most cases, CLEM involves a distinct set of sequentially used specimen preparation and labeling techniques, followed by diverse types of light and electron microscopy techniques, with specific workflows for sample transfer and relocation of regions of interest. A key advantage of sequential CLEM is the wide diversity of available microscopes: in principle, any type of microscope can be added to the workflow, provided requirements on sample preparation and handling can be met. Procedures to combine different light and electron microscopes can, however, be tedious, involving extensive manual labor, transfers, and cumbersome ROI retrieval.

## 1.4. Integrated microscopy

Microscopes that integrate a light and an electron microscope in one have been developed as early as the 1980s and a wide variety of integrated microscopes with different modalities has been reported in literature in recent years [22, 23]. Several of these have now also become commercially available. For a specific CLEM experiment, the choice between an experimental workflow with standalone microscopes or with an integrated microscope depends on a variety of factors: the precise goal and requirements of the experiment, amenable sample preparation protocols, and local availability of microscopes, probes, and expertise. If only a single or very few samples have to be carried through the CLEM workflow, adopting sample preparation protocols towards integrated inspection may not be worth the effort. On the other hand, integrated microscopes offer advantages in terms of throughput, avoiding sample contamination, achievable precision of ROI retrieval, and ease and accuracy of image correlation.

## 1.5. Integrated correlative array tomography

The advantages offered by integrated microscopy extend to volume imaging. In conventional array tomography, a tissue specimen is chemically fixated, embedded in resin, and cut into a series of ultrathin sections which are collected as ribbons on a solid substrate or on flexible, sticky Kapton tape. The sections are then

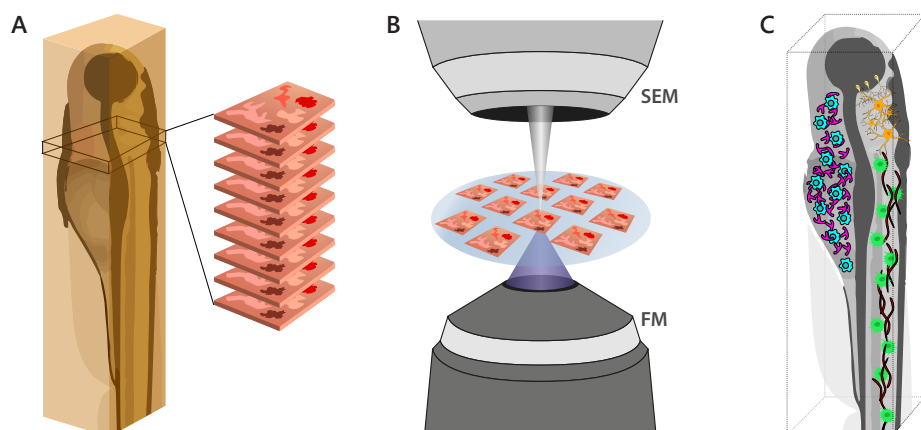


**Figure 1.1.** Conceptual overview of the integrated array tomography workflow. (A) Serial sections are cut from a resin-embedded specimen; a larval zebrafish is illustrated here as an example. (B) The sections are placed onto an ITO-coated glass slide which is mounted onto the translation stage of the integrated microscope. A series of registered EM-FM image pairs are acquired according to a semi-automated imaging pipeline. (C) The EM images are computationally aligned in 3D, revealing the structure of the zebrafish. The fluorescence data, comprising the targeted organelles, proteins, or biomolecules, is then overlaid onto the EM, resulting in a volume CLEM reconstruction of the zebrafish. Larval zebrafish illustration derived from original artwork by Lizzy Griffiths.

immunostained for imaging in a widefield or confocal fluorescence microscope, possibly in several rounds to target multiple molecules. Next, the sections are washed and reprocessed for EM with e.g. osmium tetroxide or uranyl acetate and transferred to a scanning or transmission electron microscope [24, 25]. Integrated array tomography seeks to advance this workflow by combining FM and EM acquisition with the high alignment accuracy and automation afforded by an integrated light and electron microscope. While the need for intermediate sample preparation is removed, it does, however, impose stricter constraints on the amount of heavy metal staining that can be used for EM to avoid quenching fluorophores [26, 27]. To circumvent the loss of signal without increasing the dwell time, a negative bias potential can be used to enhance the collection of backscattered electrons (Chapter ??).

The workflow for integrated correlative array tomography (iCAT; Fig. 1.1) begins by following a customized protocol for fixating, embedding, cutting, and immunolabeling a sample such that the fluorescence is maintained. Serial sections are then loaded into the integrated microscope and imaged sequentially, while an automated procedure for EM-FM registration [28] ensures consistent overlay accuracy. Custom-built alignment routines are then used to reconstruct the correlative datasets in three-dimensions. The acquisition and reconstruction procedures for integrated array tomography comprise the basis of Chapter 2.

Future applications of CLEM will demand greater precision, further automation, and higher throughput, for which iCAT offers a number of potential advantages. Above all, iCAT enables large numbers of serial sections to be sequentially and automatically imaged to generate reconstructed volumes of overlaid FM and EM datasets with matching axial resolution. Moreover, specimen warping and shrinkage, which might otherwise occur in conventional array tomography methods, is prevented due to the absence of intermediate sample preparation. This ensures a precise overlay of biological molecules and structural context at high resolution in all three dimensions. Additionally, precisely overlaid fluorescence data has the potential to vastly improve classification of ultrastructural features in EM data. While modern machine-learning-based segmentation methods (e.g. ilastik [29], SuRVoS [30]) are quite sophisticated, they nevertheless require some degree of manual annotation. Because high-accuracy overlaid correlative datasets contain, in a sense, the classification data that these methods seek to provide, such datasets could reduce the need for supervised learning while opening up new possibilities for machine learning applications such as artificial fluorescence predictions (Chapter ??).

# REFERENCES

- [1] Santiago Ramón et al. *Textura del sistema nervioso del hombre y de los vertebrados: estudios sobre el plan estructural y composición histológica de los centros nerviosos adicionados de consideraciones fisiológicas fundadas en los nuevos descubrimientos*. Vol. 1. Moya, 1899.
- [2] Stanley Finger. *Origins of neuroscience: a history of explorations into brain function*. Oxford University Press, USA, 2001.
- [3] Moritz Helmstaedter, Kevin L Briggman, and Winfried Denk. “3D structural imaging of the brain with photons and electrons”. *Current opinion in neurobiology* 18.6 (2008), pp. 633–641.
- [4] Narayanan Kasthuri et al. “Saturated reconstruction of a volume of neocortex”. *Cell* 162.3 (2015), pp. 648–661.
- [5] John G White et al. “The structure of the nervous system of the nematode *Caenorhabditis elegans*”. *Philos Trans R Soc Lond B Biol Sci* 314.1165 (1986), pp. 1–340.
- [6] Tomoko Ohyama et al. “A multilevel multimodal circuit enhances action selection in *Drosophila*”. *Nature* 520.7549 (2015), pp. 633–639.
- [7] Kerrianne Ryan, Zhiyuan Lu, and Ian A Meinertzhagen. “The CNS connectome of a tadpole larva of *Ciona intestinalis* (L.) highlights sidedness in the brain of a chordate sibling”. *Elife* 5 (2016), e16962.
- [8] David Grant Colburn Hildebrand et al. “Whole-brain serial-section electron microscopy in larval zebrafish”. *Nature* 545.7654 (2017), pp. 345–349.
- [9] Zhihao Zheng et al. “A complete electron microscopy volume of the brain of adult *Drosophila melanogaster*”. *Cell* 174.3 (2018), pp. 730–743.
- [10] Jeff W Lichtman and Joshua R Sanes. “Ome sweet ome: what can the genome tell us about the connectome?” *Current opinion in neurobiology* 18.3 (2008), pp. 346–353.
- [11] Davi D Bock et al. “Network anatomy and in vivo physiology of visual cortical neurons”. *Nature* 471.7337 (2011), pp. 177–182.
- [12] Jörgen Kornfeld and Winfried Denk. “Progress and remaining challenges in high-throughput volume electron microscopy”. *Current opinion in neurobiology* 50 (2018), pp. 261–267.
- [13] Christopher J Peddie and Lucy M Collinson. “Exploring the third dimension: volume electron microscopy comes of age”. *Micron* 61 (2014), pp. 9–19.

- [14] Kevin L Briggman and Davi D Bock. "Volume electron microscopy for neuronal circuit reconstruction". *Current opinion in neurobiology* 22.1 (2012), pp. 154–161.
- [15] Martina Schifferer et al. "Niwaki Instead of Random Forests: Targeted Serial Sectioning Scanning Electron Microscopy With Reimaging Capabilities for Exploring Central Nervous System Cell Biology and Pathology". *Frontiers in neuroanatomy* (2021), p. 79.
- [16] Kristen M Harris and John K Stevens. "Dendritic spines of CA 1 pyramidal cells in the rat hippocampus: serial electron microscopy with reference to their biophysical characteristics". *Journal of Neuroscience* 9.8 (1989), pp. 2982–2997.
- [17] Ian A Meinertzhagen and SD O'neil. "Synaptic organization of columnar elements in the lamina of the wild type in *Drosophila melanogaster*". *Journal of comparative neurology* 305.2 (1991), pp. 232–263.
- [18] Matthia A Karreman et al. "Fast and precise targeting of single tumor cells in vivo by multimodal correlative microscopy". *Journal of Cell Science* 129.2 (2016), pp. 444–456.
- [19] Matthia A Karreman et al. "Intravital correlative microscopy: imaging life at the nanoscale". *Trends in cell biology* 26.11 (2016), pp. 848–863.
- [20] Pascal De Boer, Jacob P Hoogenboom, and Ben NG Giepmans. "Correlated light and electron microscopy: ultrastructure lights up!" *Nature methods* 12.6 (2015), pp. 503–513.
- [21] Toshio Ando et al. "The 2018 correlative microscopy techniques roadmap". *Journal of physics D: Applied physics* 51.44 (2018), p. 443001.
- [22] AC Zonneville et al. "Integration of a high-NA light microscope in a scanning electron microscope". *Journal of microscopy* 252.1 (2013), pp. 58–70.
- [23] Frank Jan Timmermans and Cornelis Otto. "Contributed review: Review of integrated correlative light and electron microscopy". *Review of scientific instruments* 86.1 (2015), p. 011501.
- [24] Kristina D Micheva and Stephen J Smith. "Array tomography: a new tool for imaging the molecular architecture and ultrastructure of neural circuits". *Neuron* 55.1 (2007), pp. 25–36.
- [25] Irene Wacker and RR Schroeder. "Array tomography". *Journal of microscopy* 252.2 (2013), pp. 93–99.
- [26] Jeroen Kuipers, Pascal de Boer, and Ben NG Giepmans. "Scanning EM of non-heavy metal stained biosamples: Large-field of view, high contrast and highly efficient immunolabeling". *Experimental Cell Research* 337.2 (2015), pp. 202–207.
- [27] Christopher J Peddie et al. "Correlative super-resolution fluorescence and electron microscopy using conventional fluorescent proteins in vacuo". *Journal of structural biology* 199.2 (2017), pp. 120–131.

- [28] Martijn T Haring et al. “Automated sub-5 nm image registration in integrated correlative fluorescence and electron microscopy using cathodoluminescence pointers”. *Scientific reports* 7.1 (2017), pp. 1–9.
- [29] Christoph Sommer et al. “Ilastik: Interactive learning and segmentation toolkit”. *2011 IEEE international symposium on biomedical imaging: From nano to macro*. IEEE. 2011, pp. 230–233.
- [30] Imanol Luengo et al. “SuRVoS: super-region volume segmentation workbench”. *Journal of Structural Biology* 198.1 (2017), pp. 43–53.



# 2

## INTEGRATED ARRAY TOMOGRAPHY FOR 3D CORRELATIVE LIGHT AND ELECTRON MICROSCOPY

Volume electron microscopy (EM) of biological systems has grown exponentially in recent years due to innovative large-scale imaging approaches. As a standalone imaging method, however, large-scale EM typically has two major limitations: slow rates of acquisition and the difficulty to provide targeted biological information. We developed a 3D image acquisition and reconstruction pipeline that overcomes both of these limitations by using a wide-field fluorescence microscope integrated inside of a scanning electron microscope. The workflow consists of acquiring large field of view fluorescence microscopy (FM) images, which guide to regions of interest for successive EM (integrated correlative light and electron microscopy). High precision EM-FM overlay is achieved using cathodoluminescent markers. We conduct a proof-of-concept of our integrated workflow on immunolabelled serial sections of tissues. Acquisitions are limited to regions containing biological targets, expediting total acquisition times and reducing the burden of excess data by tens or hundreds of GBs.

---

This chapter has been published as: Ryan Lane et al. "Integrated array tomography for 3D correlative light and electron microscopy". *Frontiers in neuroscience* (2022).

## 2.1. Introduction

A central objective within neuroscience and cell biology is to produce high-resolution (1–10 nm), three-dimensional reconstructions of biological specimen. Volume electron microscopy (EM) is the preferred imaging method in this arena because of its unique ability to resolve features across a wide spectrum of spatial scales [2, 3]. While EM provides highly relevant structural information and precise localization of targets, immunogold labeling can only be visualized at high resolution, and in Tokuyasu labeling section areas are typically limited to 0.01 mm<sup>2</sup> for analysis [4, 5]. Fluorescence microscopy (FM) provides biologically relevant information by tagging specific biomolecules with fluorescent labels at large scale [6]. Regions of interest (ROI) can in this way be quickly and reliably identified for subsequent high magnification EM imaging. The information from these two imaging modalities are combined in correlative light and electron microscopy (CLEM). ROI retrieval across different microscopes is, however, nontrivial at large scales, particularly when spread across multiple sections [7, 8, 9, 10, 11]. Other challenges associated with CLEM include the reliance on fiducial markers and intermediate sample preparation [12, 13]. One means of combating these challenges is by merging these separate imaging systems into a single, integrated fluorescence and electron microscope [14]. By detecting fluorescence expression *in-situ*, it can further be decided in an automated fashion which areas to scan at high magnification and which areas to omit for the sake of higher throughput [15]. For array tomography applications, ROIs can be targeted with increasing magnification through a sequence of feedback loops [16]. Similarly, strategies for rapidly screening sections have been developed for sequential CLEM to limit volume acquisitions to select ROI [17, 18].

Despite these potential benefits, an integrated microscope presents new challenges. In conventional array tomography sample preparation, the sample is eluted and restained between imaging methods [19]. Hence, there is no need to preserve fluorescence labelling, which allows for post-staining to enhance EM contrast [20, 21]. The traditional way to compensate for diminished contrast is to boost the EM signal by increasing the dwell time per pixel, but this comes at the expense of throughput. An additional complication in integrated CLEM is electron-beam-induced quenching of the fluorescence [22]. This imposes the constraint that the fluorescence in a given area must be acquired prior to exposure from the electron beam, which prohibits uniformly pre-irradiating the sample with the electron beam to enhance and stabilize contrast [23]. Conversely, in conventional serial-section EM, there are scarce constraints regarding the number of times a particular sample may be scanned, making possible approaches such as that by Hildebrand et al. [24].

Our goal is to establish a workflow capable of quickly and efficiently rendering three-dimensional CLEM volumes from serial sections in such a way as to overcome these challenges. Three key initiatives steered the design of our integrated correlative array tomography (iCAT) procedure. First, to prevent damaging or quenching of the fluorescence signal via electron-beam irradiation, each FM field of view must be acquired prior to EM exposure. Second, to compensate for the reduced

application of contrast agents, backscattered electron (BSE) collection efficiency is enhanced via a negative stage bias, allowing for higher throughput [25, 26]. Finally, a high precision EM-FM overlay is facilitated by the use of cathodoluminescent (CL) points, which eliminates the need for artificial fiducial markers [27]. An alignment method was then developed to reconstruct the correlative image stack. Islets of Langerhans from both rat and zebrafish pancreas tissue were chosen to prototype the imaging and reconstruction workflows. By offering a more holistic visualization of tissue, our integrated approach to 3D CLEM could lead to greater insights in (patho)biology [28].

## 2.2. Material & methods

### 2.2.1. Tissue and sample preparation

Rat pancreas was prepared as follows: fresh pancreas was cut from an 83 day old rat into small pieces and fixed in 4% paraformaldehyde (PFA; Merck) + 0.1% glutaraldehyde (GA; Polysciences) as described in Ravelli et al. [29]. A complete zebrafish larva (120 hpf) was fixed in 2% PFA + 2% GA. Both samples were post-fixed in 1% osmium tetroxide and 1.5% potassium ferricyanide in 0.1 M cacodylate buffer, dehydrated through ethanol and embedded in EPON (Serva). 100 nm serial sections were cut and placed onto formvar-covered ITO-coated glass coverslips (Optics Balzers). Immunolabeling was performed as described previously [23]. Samples were etched with 1% periodic acid for 10 min, followed by a 30 min blocking step: 1% bovine serum albumin (BSA; Sanquin, Netherlands) in tris-buffered saline (TBS), pH 7.4. Next, anti-insulin was incubated for 2 hr (guinea pig; 1:50, Invitrogen, PA1-26938, RRID: AB\_794668, for rat pancreas and anti-insulin; 1:100, Abcam, ab210560, for zebrafish pancreas), followed by washing and subsequent incubation for 1 hr with biotinylated secondary antibody (donkey-anti-guinea pig; 1:400, Jackson ImmunoResearch, for rat pancreas and goat-anti-rabbit; 1:400, Dako, for zebrafish pancreas) followed by washing steps. Finally, streptavidin conjugated AF594 (1:100, Jackson ImmunoResearch, for rat pancreas) and streptavidin conjugated TRITC (1:100, Jackson ImmunoResearch, for zebrafish pancreas) were added for 1 hr followed by washing.

### 2.2.2. Digital light microscopy

The sections, after being placed on the ITO-coated glass slide, are imaged at 30X magnification ( $\sim 7 \mu\text{m}/\text{px}$ ) using a VHX-6000 digital light microscope (Keyence) operating in reflection mode. To capture every section on the 22 mm  $\times$  22 mm ITO-coated glass slide, a 3  $\times$  3 grid of RGB images is acquired and automatically stitched together.

### 2.2.3. Integrated microscopy

The integrated microscope is a widefield SECOM fluorescence microscope (Delmic B.V.) retrofitted into the vacuum chamber of a Verios 460 SEM (Thermo Fisher Scientific) [14, 30]. The microscopes share a common optical axis, translation stage,

and control software. FM images are obtained with 10 s exposures, recorded by a Zyla 4.2 sCMOS camera (Andor - Oxford Instruments). Excitation wavelengths of 405 nm and 555 nm are used to excite Hoechst and AF594. The SECOM is equipped with a CFI S Plan Fluor ELWD 60XC (0.70 NA) objective (Nikon), which allows for long working distance imaging (1.8–2.6 mm), to prevent electrical breakdown in vacuum, which must be accounted for due to the presence of high electric fields induced by the stage bias [31].

SEM imaging is conducted in two rounds: (1) low-magnification (38 nm/px) scans accompanying each fluorescent acquisition; (2) high-magnification (5 nm/px) acquisitions on ROI identified by fluorescence expression. Both low and high magnification imaging are performed at 2.5 keV primary beam energy with a  $-1$  kV bias potential applied to the sample stage such that the landing energy is 1.5 keV, which proved optimal for  $\sim 100$  nm sections. The negative potential bias enhances the backscattered electron (BSE) signal, which is collected by the insertable concentric backscattered detector (Thermo Fisher Scientific) [26].

## 2.2.4. Alignment and reconstruction software

Image data from the integrated microscope is uploaded to a local storage server running an instance of render-ws,<sup>1</sup> a collection of open-source web services for rendering transformed image tiles. The tiles and their respective metadata are organized into stacks, configured as MongoDB databases. The alignment routines are arranged in a series of Jupyter notebooks,<sup>2</sup> which parse the image metadata for the EM-FM overlay as well as make calls to render-ws via a python wrapper (render-python<sup>3</sup>). EM image stitching and volume alignment are based on the scale-invariant feature transform (SIFT)—an algorithm designed to detect and match local features in corresponding images [32]. SIFT features are stored in render-ws databases where they can be processed by BigFeta,<sup>4</sup> a linear least squares solver for scalable 2D and 3D image alignment based on point correspondences. CLEM datasets are ultimately exported to CATMAID [33] for google-maps-like visualization. 3D visualizations are done in Fiji [34] using the Volume Viewer plugin.<sup>5</sup>

## 2.3. Results

### 2.3.1. Section detection and *in-situ* navigation

Simple navigation between serial sections within the integrated microscope is crucial. Following joint EM-FM sample preparation (Figure 2.1A), the sections are imaged by the digital light microscope (DLM) (Figure 2.1B). To facilitate navigation within the integrated microscope (Figure 2.1C), the resulting overview image is used for detecting the boundaries of each section on the ITO-coated glass sub-

---

<sup>1</sup><https://github.com/saalfeldlab/render>

<sup>2</sup><https://github.com/hoogenboom-group/iCAT-workflow>

<sup>3</sup><https://github.com/AllenInstitute/render-python>

<sup>4</sup><https://github.com/AllenInstitute/BigFeta>

<sup>5</sup><https://imagej.net/plugins/volume-viewer>

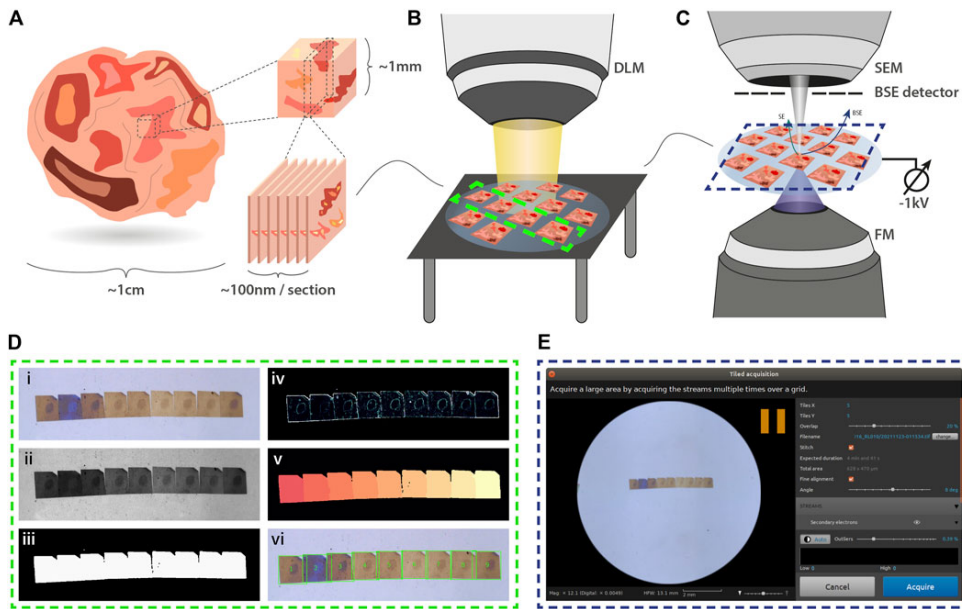


**Figure 2.1.** Integrated array tomography. (A) Ultrathin sections are prepared for simultaneous FM and EM imaging. (B) An overview image of the sections on the ITO-coated glass slide is then acquired by a digital light microscope (DLM). (C) Next, the sample is transferred to the integrated microscope for CLEM imaging. SEM imaging is performed using a  $-1$  kV bias potential applied to the sample stage to enhance BSE collection from the non-post-stained sections. (D) The overview image obtained by the DLM is used for instance segmentation of the serial sections. Descriptions of the image processing steps (i-vi) is provided in the main text. (E) The section overview image and bounding box coordinates of each serial section are fed to the microscope software to facilitate navigation.

strate via a segmentation routine<sup>6</sup> (Figure 2.1D). The overview image (inset i) is first contrast enhanced and converted to grayscale (inset ii). Intensity-based thresholding is used to create a binary mask image (inset iii), which is then applied to the grayscale image. To retrieve outlines of the section boundaries, the gradient is computed (inset iv). Watershed segmentation is then implemented by flooding the gradient image with a number of markers equal to the number of serial sections in the image (inset v). The resulting labelled image (inset vi) then serves as input for navigation using a plugin within Odemis,<sup>7</sup> the open-source software that controls the microscope (Figure 2.1E).

<sup>6</sup><https://github.com/hoogenboom-group/secdetect>

<sup>7</sup><https://github.com/delmic/odemis>

### 2.3.2. Targeted correlative acquisition of an individual region of interest

To identify ROI in the integrated microscope for subsequent EM acquisition, the correlative imaging scheme is engineered to obtain fluorescence overviews of each section, undamaged by the electron beam. The workflow starts by acquiring a FM and low-magnification EM image tile (Figure 2.2A). The FM tile is acquired prior to the EM tile to preserve the fluorescence signal. An automated registration routine guided by cathodoluminescent (CL) spots is then run to register the image pair [27]. This sequence of correlative imaging is automatically repeated in a grid-like pattern, encompassing the entire section. FM image tiles are acquired with a 20% overlap such that they can be stitched together to allow for fluorescence-based ROI detection within each section (Figure 2.2B). The field width of the EM tile ( $\sim 140 \mu\text{m}$ ) is chosen such that it spans the maximum extent possible without entering the overlap region of the neighboring FM image tiles,

$$w_{EM} = w_{FM} - 2o_{FM}w_{FM} \quad (2.1)$$

where  $w_{EM}$  and  $w_{FM}$  are the respective EM and FM fields of view, and  $o_{FM}$  is the overlap between adjacent FM tiles. In this way EM-FM registration is performed over as large an area as possible, while avoiding bleaching of the fluorescence. Fluorescence imaging of the entire section prior to EM would fulfil the same objective while circumventing the need for gaps between low-magnification EM image tiles. This would require manually registering the tilesets, however, as the transformation obtained from the CL registration procedure is unique to each image pair.

Fluorescence expression is then used to target areas for additional EM imaging at higher magnification (5 nm/px) (Figure 2.2C). The ROI is manually navigated to via stage translation, whereby an automated tileset acquisition is initiated (Figure 2.2D). The tiles are spaced with a 10–15% overlap such that they can be stitched during post-processing. The correlative imaging pipeline is then repeated on the remaining serial sections.

### 2.3.3. 2D Stitching and correlation

Overlaying the fluorescence onto the high-magnification EM requires correlating the datasets across different modalities and spatial scales. Each FM tile is first overlaid onto the corresponding low-magnification EM tile using the metadata generated by the CL registration procedure. A grid of CL spots is recorded with the camera of the fluorescence microscope in the absence of excitation light (Figure 2.3A). The appropriate affine transformation is calculated by localizing each CL spot and matching it with the known position of the electron beam (“cross-modal” registration) [27]. The stage coordinates are extracted to then correlate and position each image pair in the tileset (Figure 2.3A).

The high-magnification EM tileset is stitched independently of both the FM and low-magnification EM tiles (Figure 2.3B). Stage coordinates are used to first establish a set of potential neighboring tiles. For each tile, SIFT features are extracted and matched between the candidate neighbors. Affine transformation parameters

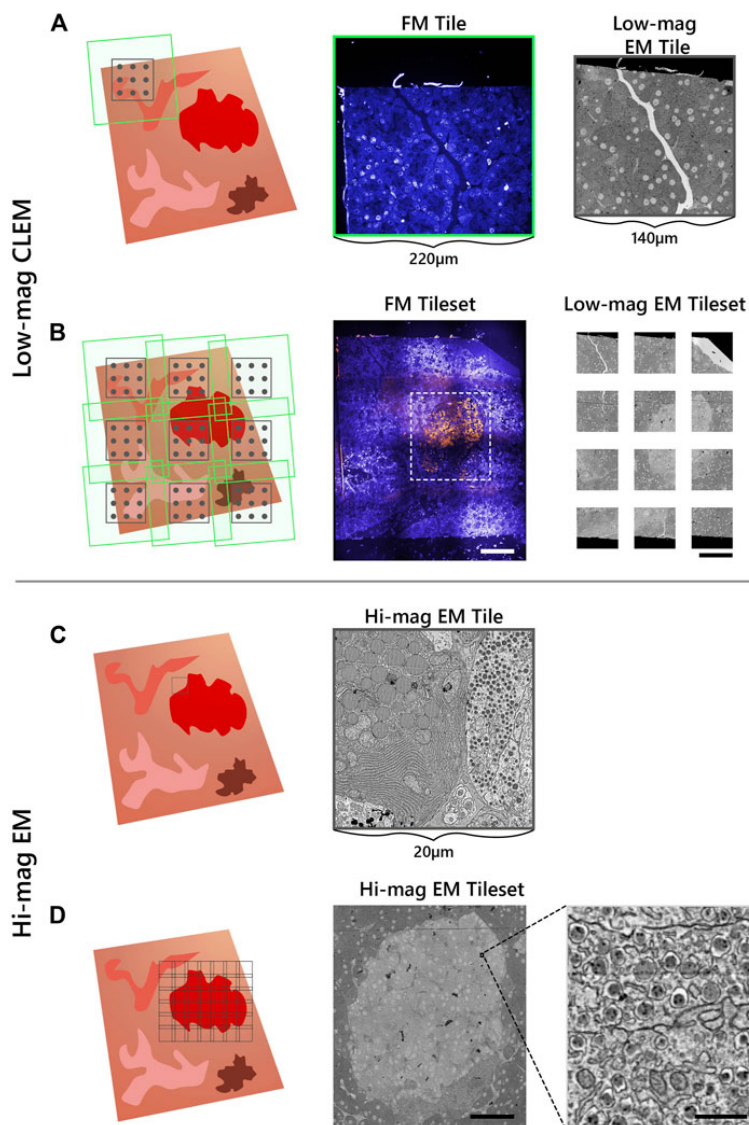


**Figure 2.2.** Integrated array tomography provides efficient, high-precision EM-FM imaging without bleaching of the fluorescence. (A) Acquisition of correlative FM (green outline) and low-magnification EM (black outline) images, followed by a registration procedure involving CL spots (grey circles) to register the image pair. (B) The stage is translated in a grid-like fashion such that there is sufficient overlap between neighboring FM image tiles—leaving a gap between adjacent EM tiles. (C) The fluorescence signal is used to identify targets for subsequent EM imaging (black outline). (D) The target ROI is captured by an automated tileset of high magnification EM tiles. Scalebars: (B) 100  $\mu\text{m}$ ; (D) 50  $\mu\text{m}$  (inset, 0.5  $\mu\text{m}$ ).



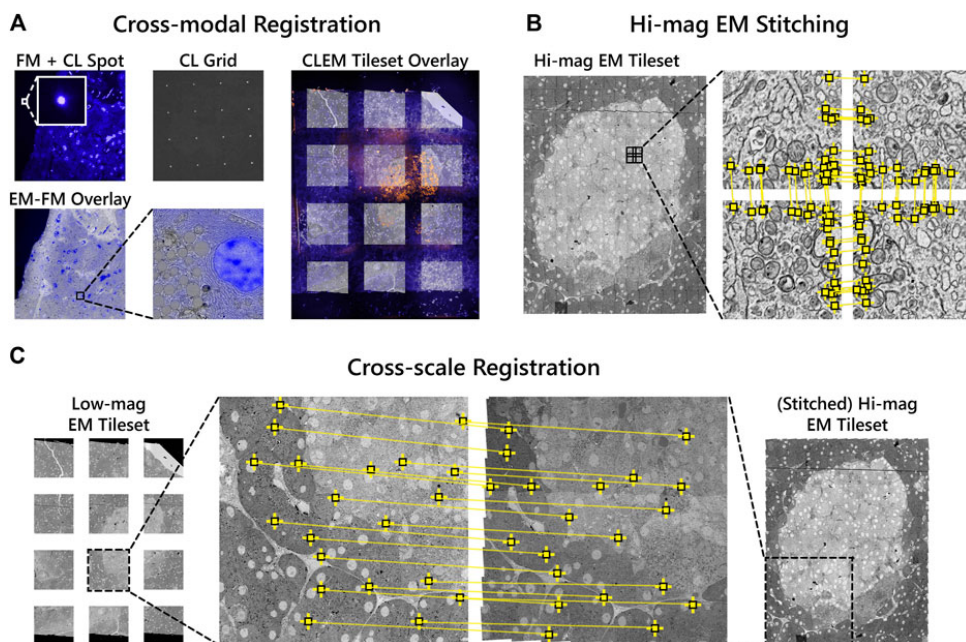


**Figure 2.3.** Correlative alignment routine registers tilesets across modalities and scales. (A) Automated registration procedure for registering FM and low-magnification EM image pairs using CL spots. FM tiles are then overlaid onto the low-magnification EM tiles of each section. (B) SIFT features (yellow squares) are extracted and used to stitch together neighboring high-magnification EM tiles within each section. (C) Low-magnification EM images are registered to the corresponding area of the stitched together high-magnification EM tileset. The low-magnification tiles thereby serve as a reference to ultimately overlay the fluorescence onto the high-magnification EM.

for each tile are then estimated by minimizing the squared distance between corresponding features [35, 36].

Next, the low-magnification image tiles are registered to the corresponding area of the stitched high-magnification EM tileset (“cross-spatial” registration, Figure 2.3C). Stage coordinates are used to determine the set of high-magnification tiles that overlap with each low-magnification tile. A composite image of the overlapping tiles is rendered, processed with SIFT, and matched with the features in the low-magnification tile. The affine transformation computed from the feature matching is then propagated to each of the FM tiles such that they are overlaid onto the high-magnification EM tileset. In this way, the low-magnification EM serves as a proxy to correlate the fluorescence to the high-magnification EM. The overlay accuracy is reduced in the areas between low-magnification tiles where the transformation is extrapolated (Supplementary Figure 3.S1A – F). This can be corrected for via (manual) landmark registration by e.g. aligning the Hoechst signal to nuclei recognized in the EM using software such as ec-CLEM [37], which is routinely



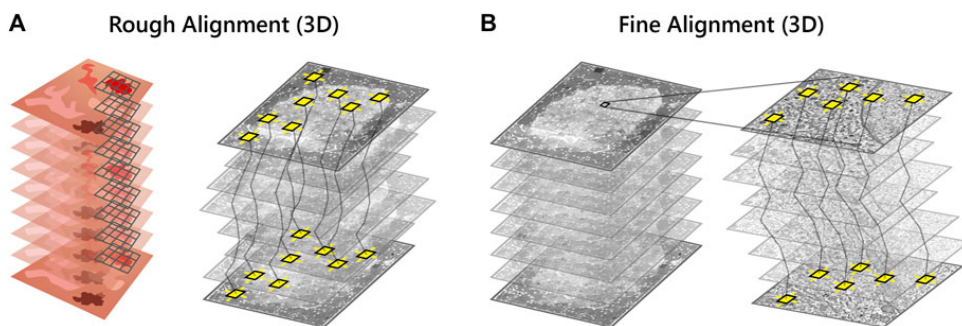


**Figure 2.4.** Volume reconstruction of the high-magnification EM stack. (A) SIFT features (yellow squares) are used to roughly align the high-magnification EM stack in  $z$ . A downsampled image of each section is rendered as the full resolution EM tileset is too large (several GB) for feature extraction. (B) The EM stack alignment is refined by least squares optimization of the displacement between matched features.

used for image registration in sequential CLEM experiments [38, 39, 40]. In general, the overlay accuracy cannot be expected to be below the pixel size of the low magnification EM.

### 2.3.4. Correlative 3D reconstruction

A robust and scalable solution is required for volume alignment of the high-magnification EM stack, the “backbone” of the multimodal dataset. The stitched sections are downsampled and roughly aligned in  $z$  (Figure 2.4A) to facilitate feature mapping between image tiles in adjacent sections. A system of linear equations consisting of SIFT features is then solved to finely align the image stack in 3D (Figure 2.4B) [36]. The features extracted during stitching are reused, enabling a faster and more efficient reconstruction of the EM volume.

The 2D correlative alignment procedure (Figure 2.3) is then run on each section, mapping the fluorescence onto the high-magnification EM volume. The nine serial sections of rat pancreas were thereby used to realize a proof-of-concept of the iCAT workflow (Figure 2.5A). An islet of Langerhans was identified from anti-insulin immunofluorescence of AF594 and chosen for subsequent, high-magnification EM imaging (Figure 2.5B). The fluorescence data clearly delineates the endocrine region from the surrounding exocrine tissue, which is characterized by dense endoplasmic reticulum (ER) and the absence of insulin labeling (Figure 2.5C). Although it was chosen as a nuclear marker, Hoechst also binds to the RNA present in the ER. The endocrine region, in contrast, is characterized by an abundance of insulin-secreting beta cells with distinct nuclei. The high EM-FM registration accuracy afforded by iCAT enables a clear distinction between different types of granules present in the endocrine tissue (Figure 2.5D). Discerning insulin from other hormone granules is nontrivial as all are roughly 100 nm in diameter. Making this differentiation from EM data alone requires expert-level interpretation.

By limiting high-magnification EM to only the islet, the total imaging volume is

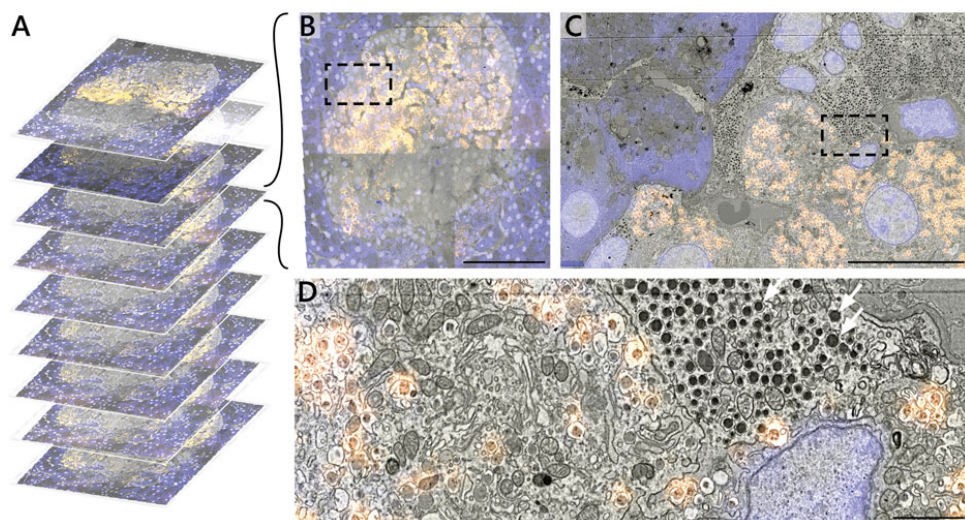


**Figure 2.5.** Correlative reconstruction of nine sections of pancreas. (A) 2D and 3D alignment routines are combined to yield a CLEM stack of nine serial sections of rat pancreas tissue. (B – D) CLEM imaging of the islet of Langerhans at varying spatial resolution. Hoechst (blue) and AF594 (orange) fluorescence signals are superimposed onto the EM ultrastructure. The AF594 signal, in particular, facilitates recognition of insulin granules from e.g. non-fluorescent glucagon granules (white arrows, D). Scale bars: (B) 50  $\mu\text{m}$ ; (C) 5  $\mu\text{m}$ ; (D) 1  $\mu\text{m}$ . Raw data at full resolution is available via Nanotomy.

reduced by a factor  $\sim 10$  with respect to the full section volume (0.03  $\text{mm}^2$  per islet vs 0.4  $\text{mm}^2$  per section). Similar reductions are realized in the total dataset size (0.1 vs  $\sim 1$  TB) easing data management requirements. This initial proof of concept was designed around only a limited number of serial sections to more efficiently optimize each procedure in the workflow.

### 2.3.5. Proof of concept on zebrafish pancreas tissue

To demonstrate the scalability of the workflow, we applied it to a larger volume of larval zebrafish (Figure 2.6). The Hoechst signal was useful in identifying the exocrine region of the pancreas (Figure 2.6B) as the insulin immunofluorescence from TRITC was weak. TRITC was chosen for its stronger fluorescence in vacuum compared to Alexa dyes (manuscript in preparation); potential causes for the weak immunofluorescence in the zebrafish pancreas are still under investigation. The exocrine region, encompassing an islet of Langerhans, together with the underlying muscle tissue was selected for high magnification EM. The reconstruction of the CLEM volume was cropped to remove the background fluorescence in the swim bladder (Figure 2.6C). Sub-stacks within the correlative volume were then extracted for further analysis (Figures 2.6D, G). Note that the ultrastructure is better preserved in most tissues than in the islet (Figure 2.6H, I), a phenomenon previously seen in other species (unpublished results).

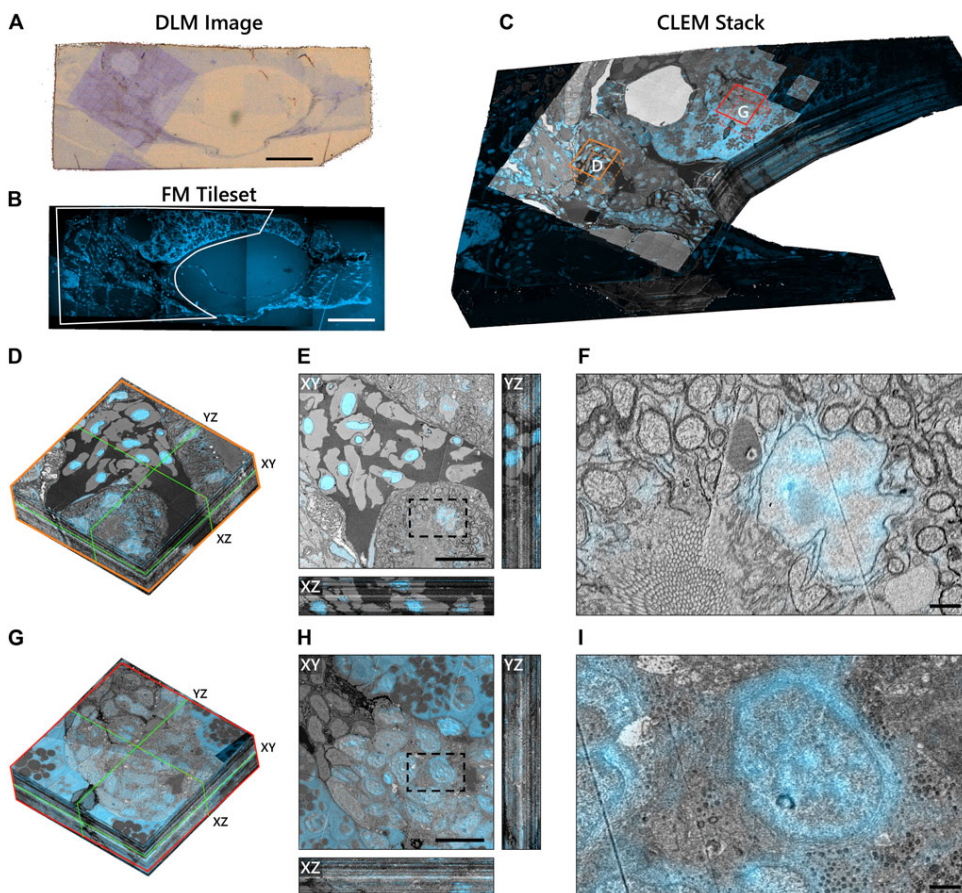


**Figure 2.6.** Integrated correlative array tomography applied to 63 serial sections of zebrafish pancreas. (A) Contrast-enhanced optical image of an individual serial section obtained by the DLM. The section was re-acquired post-EM imaging, revealing the region of interest irradiated by the electron beam. The biological material can be seen in pale blue in contrast with the bare EPON (brown background). (B) Hoechst signal of an individual serial section, outlining (white) the portion of the tissue shown in (C). (C) CLEM volume of the zebrafish tissue cropped to the ROI selected for high-magnification EM imaging—plus a portion of the surrounding fluorescence signal. Sub-stacks for inspection are denoted by orange (D – F) and red (G – I) boxes. (D) 3D sub-stack of muscle tissue within the zebrafish pancreas. Green lines indicate orthoslices of the XY, XZ, and YZ planes shown in (E). (F) Zoomed-in region of the XY plane showing high-precision FM overlay of Hoechst onto a cell nucleus. (G – I) Same as in (D – F), but for an islet of Langerhans. Ill-defined cell and organelle membranes in (H) and (I) indicate suboptimal preservation of the ultrastructure in this region of the pancreas. Scale bars: (A, B) 100  $\mu\text{m}$ ; (E, H) 10  $\mu\text{m}$ ; (F, I) 1  $\mu\text{m}$ . Raw data at full resolution is available via Nanotom.

We generally observe high EM-FM overlay precision as evidenced by the Hoechst signal confined to the nuclear envelope in the muscle tissue (Figure 2.6E, F). The registration accuracy does, however, exhibit variability in several sections—more so than is seen in the rat pancreas tissue where it appears limited to the gaps between low-magnification EM tiles. In these instances, the inaccuracy stems from a malfunction in the CL registration procedure itself (Supplementary Figure 3.S1G–N). Variations in the EM image intensity, particularly in the islet, can also be observed for a number of sections (Figure 2.6H: XZ and YZ cross-sections). We attribute these artifacts primarily to ultrastructure preservation as they do not appear to be as prevalent in the muscle tissue. While the SEM imaging parameters and detection settings were held constant throughout the acquisition, day-to-day changes in the environment (e.g. temperature, humidity levels) may have varied.

In total, 66 sections were prepared, of which three ( $z = 9, 10, 34$ ) were discarded due to excess surface debris. The omission of consecutive sections was mitigated by extending the SIFT feature depth search from 2 to 3 such that sections  $z = 8$  and  $z = 11$  could be registered. Total acquisition times for low-magnification CLEM and high-magnification EM were 7.2 hr and 71 hr respectively, versus 335 hr for full section imaging at high-magnification.

## 2.4. Discussion

A new workflow for integrated array tomography for the semi-automated acquisition and reconstruction of volume CLEM data is presented. High-resolution EM is limited to select ROI by targeting areas based on fluorescence expression. This not only expedites acquisition time, but eases the burden on data management requirements. Interpretation of EM data is in turn facilitated by the addition of fluorescent labels. The workflow demonstrated here extends the work of Liv et al. [14], which introduced the integrated microscope, and Haring et al. [27], which presented the fiducial-free CL registration procedure, to targeted correlative imaging of serial sections. Gabarre et al. [16] presented an alternative method for integrated array tomography in which light microscopy and EM are combined to localize structures through a series of feedback loops. Our approach differs in several ways. First, fluorescence imaging is done *in-vacuo* as opposed to transmitted light microscopy done at ambient pressure. This allows for more automated EM-FM (or EM-LM) overlay, as the CL registration procedure can only be done in high vacuum [27]. Additionally, the multi-modal alignment methodology conceived here offers a more scalable solution for generating volumetric CLEM data. Integrated array tomography was inspired in part by the multi-scale approach of Hildebrand et al. [24], in which full brain EM imaging of a larval zebrafish was conducted by selecting ROI for subsequent acquisition based on inspection between imaging rounds. In this work, conversely, ROI are identified by *in-situ* fluorescence, bypassing the need for post-processing and alignment between magnification scales.

On-section immunofluorescence and fluorescent staining constitute viable options for FM imaging of resin-embedded sections in high vacuum. Pancreas tissue in particular is well-suited for immunofluorescence due to the prevalence of



insulin epitopes. While in both nature and technique development, immunolabeling approaches are always dependent on the capacity for antibodies and epitopes to interact, this is typically inefficient for most antibodies, and particularly so for EPON-embedded sections. We find that approximately 1 in 10 antibodies tested in our lab are applicable for EPON labeling. While acrylic resins (e.g. Lowicryl, LR White) have been shown to be more compatible with immunolabeling, a trade-off must be made between the strength of the fluorescence signal and the quality of the ultrastructure [41, 42]. Complications with serial sectioning and ultrastructure preservation (beyond that shown in the zebrafish pancreas) arose when experimenting with Lowicryl; hence EPON was selected as the embedding medium for this study.

Probes typically used for live FM, such as fluorescent proteins, are likewise incompatible with conventional EM sample preparation techniques [12]. Although protocols have been developed for retaining fluorescence post-embedding [43, 41, 44, 45], the same compromises exist between fluorescence retention and ultrastructure preservation. Fluorescent proteins have the additional limitation that the specimen must be genetically modified, rendering them unsuitable for use in native animals and humans. In-resin fluorescence preservation thus remains a challenge—only made more difficult by imposing high vacuum conditions, which may lower fluorescence intensities for biological probes typically optimized for use in aqueous environments [44]. We are nevertheless confident that future developments in fluorescent proteins and embedding media will present compelling opportunities to apply integrated array tomography to a variety of biological questions.

We foresee that the multimodal datasets obtained using this method will be instrumental in forthcoming machine learning applications [46, 47, 48]. Thus far, applications of registered EM-FM datasets appear to be limited to facilitating registration of sequential CLEM data using artificial predictions for the fluorescence signal [49, 50]. Volume EM datasets, particularly in connectomics, are now routinely segmented via deep convolutional neural networks [51, 48]. Acquisition rates and manual annotation of datasets, however, both serve as bottlenecks for reconstructing dense networks of cells and organelles [3]. Given its ability to provide labeled biological information as well as reduce imaging volumes to select regions, integrated array tomography is poised to deliver significant gains in this arena.

Future work will be directed towards further refinement and automation. The CL registration procedure could be made more robust by illuminating the sample with a greater number of CL spots or by increasing the camera integration time. Updates to the alignment software could furthermore allow for the distortion field correction used in Haring et al. [27] to achieve sub-5 nm overlay precision. Cutting sections manually remains a significant bottleneck for throughput, as it is prone to error and requires expert training [52]. We expanded from a single section to nine, to 63, and have now placed more than 100 serial sections onto ITO-coated coverslips. Increasing beyond  $\sim 10\ \mu\text{m}$  of biological material, however, is cumbersome without more sophisticated sectioning techniques such as automated tape-collecting ultramicrotome (ATUM) [53] or magnetic collection [54]. These may in-

introduce their respective complications; ATUM, for example, is designed to collect sections on (opaque) Kapton tape. More extensive automation strategies can alternatively be applied to the correlative imaging pipeline. Delpiano et al. [15] devised a way to automatically detect fluorescent cells using an integrated light and electron microscope. We envision a workflow for fully automated integrated array tomography in which fluorescent ROIs are automatically recognized, navigated to, and acquired, rendering three-dimensional CLEM datasets tailored to answer the specific biological research question.

## 2.5. Supplementary material

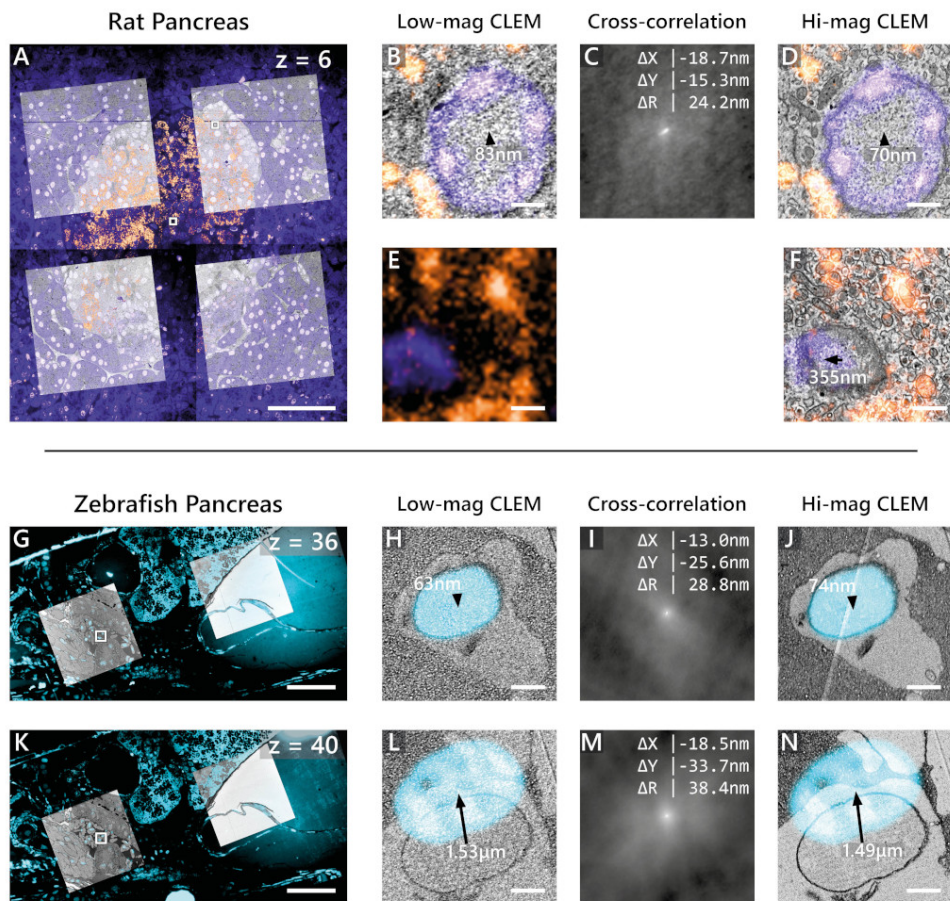


**Figure 3.S1.** Reduced overlay accuracy due to extrapolation and errors in the CL registration procedure. Overlay (in)accuracy is a combination of the errors in the cross-modal and cross-spatial registration procedures. (A) Partial low-magnification CLEM tileset of rat pancreas from which features inside (B – D) and outside (E – F) a low-magnification EM tile were selected to assess the overlay accuracy (denoted by white squares). (B) Cross-modal registration error for a cell nucleus in low-magnification CLEM, measured by calculating the centroid of the nucleus in both modalities and computing the relative displacement. (C) Cross-spatial registration error as measured by the phase correlation between the low and high-magnification EM. (D) Sub-100 nm overlay accuracy for the cell nucleus in high-magnification CLEM. (E – F) Same as in (B) and (D) for a cell nucleus acquired outside of a low-magnification EM tile. Overlay accuracy is reduced to several hundred nanometers due to the imprecision incurred by extrapolating the cross-modal registration. (Continued on next page...)

**Figure 3.S1.** (G) Partial low-magnification CLEM tileset of zebrafish pancreas from a section in which the CL registration procedure achieved the expected precision. (H – J) Same as in (B – D) but for a nucleus in the zebrafish pancreas. (K – N) Same as in (G – J) but for the section with the lowest apparent overlay accuracy (1.5  $\mu\text{m}$ ). The inaccuracy is dominated by an error in the cross-modal registration as the phase correlation (M) shows a sub-50 nm translation. Possible causes for the error include poor CL spot localization due to noise in the CL signal. Scale bars: (A) 50  $\mu\text{m}$ ; (B, D, E, F) 0.5  $\mu\text{m}$ ; (G, K) 50  $\mu\text{m}$ ; (H, J, L, N) 1  $\mu\text{m}$ .



# REFERENCES

- [1] Ryan Lane et al. “Integrated array tomography for 3D correlative light and electron microscopy”. *Frontiers in neuroscience* (2022).
- [2] Christopher J Peddie and Lucy M Collinson. “Exploring the third dimension: volume electron microscopy comes of age”. *Micron* 61 (2014), pp. 9–19.
- [3] Jörgen Kornfeld and Winfried Denk. “Progress and remaining challenges in high-throughput volume electron microscopy”. *Current opinion in neurobiology* 50 (2018), pp. 261–267.
- [4] Willisa Liou, Hans J Geuze, and Jan W Slot. “Improving structural integrity of cryosections for immunogold labeling”. *Histochemistry and cell biology* 106.1 (1996), pp. 41–58.
- [5] Carolien Van Rijnsoever, Viola Oorschot, and Judith Klumperman. “Correlative light-electron microscopy (CLEM) combining live-cell imaging and immunolabeling of ultrathin cryosections”. *Nature methods* 5.11 (2008), pp. 973–980.
- [6] Ben NG Giepmans et al. “The fluorescent toolbox for assessing protein location and function”. *science* 312.5771 (2006), pp. 217–224.
- [7] Roman S Polishchuk et al. “Correlative light-electron microscopy reveals the tubular-saccular ultrastructure of carriers operating between Golgi apparatus and plasma membrane”. *The Journal of cell biology* 148.1 (2000), pp. 45–58.
- [8] Derron Bishop et al. “Near-infrared branding efficiently correlates light and electron microscopy”. *Nature methods* 8.7 (2011), pp. 568–570.
- [9] Matthia A Karreman et al. “Correlating intravital multi-photon microscopy to 3D electron microscopy of invading tumor cells using anatomical reference points”. *PloS one* 9.12 (2014), e114448.
- [10] Lucy M Collinson, Elizabeth C Carroll, and Jacob P Hoogenboom. “Correlating 3D light to 3D electron microscopy for systems biology”. *Current Opinion in Biomedical Engineering* 3 (2017), pp. 49–55.
- [11] Daniel G Booth et al. “SuperCLEM: an accessible correlative light and electron microscopy approach for investigation of neurons and glia in vitro”. *Biology open* 8.5 (2019), bio042085.
- [12] Pascal De Boer, Jacob P Hoogenboom, and Ben NG Giepmans. “Correlated light and electron microscopy: ultrastructure lights up!” *Nature methods* 12.6 (2015), pp. 503–513.

- [13] Matthia A Karreman et al. "Intravital correlative microscopy: imaging life at the nanoscale". *Trends in cell biology* 26.11 (2016), pp. 848–863.
- [14] Nalan Liv et al. "Simultaneous correlative scanning electron and high-NA fluorescence microscopy". *PloS one* 8.2 (2013), e55707.
- [15] J Delpiano et al. "Automated detection of fluorescent cells in in-resin fluorescence sections for integrated light and electron microscopy". *Journal of microscopy* 271.1 (2018), pp. 109–119.
- [16] Sergio Gabarre et al. "A workflow for streamlined acquisition and correlation of serial regions of interest in array tomography". *BMC biology* 19.1 (2021), pp. 1–15.
- [17] Agnes Burel et al. "A targeted 3D EM and correlative microscopy method using SEM array tomography". *Development* 145.12 (2018), dev160879.
- [18] Paolo Ronchi et al. "High-precision targeting workflow for volume electron microscopy". *Journal of Cell Biology* 220.9 (2021), e202104069.
- [19] Kristina D Micheva and Stephen J Smith. "Array tomography: a new tool for imaging the molecular architecture and ultrastructure of neural circuits". *Neuron* 55.1 (2007), pp. 25–36.
- [20] Michael L Watson. "Staining of tissue sections for electron microscopy with heavy metals". *The Journal of Cell Biology* 4.4 (1958), pp. 475–478.
- [21] Juan Carlos Tapia et al. "High-contrast en bloc staining of neuronal tissue for field emission scanning electron microscopy". *Nature protocols* 7.2 (2012), pp. 193–206.
- [22] Aditi Srinivasa Raja et al. "Electron-Beam Induced Luminescence and Bleaching in Polymer Resins and Embedded Biomaterial". *Macromolecular bioscience* (2021), p. 2100192.
- [23] Jeroen Kuipers, Pascal de Boer, and Ben NG Giepmans. "Scanning EM of non-heavy metal stained biosamples: Large-field of view, high contrast and highly efficient immunolabeling". *Experimental Cell Research* 337.2 (2015), pp. 202–207.
- [24] David Grant Colburn Hildebrand et al. "Whole-brain serial-section electron microscopy in larval zebrafish". *Nature* 545.7654 (2017), pp. 345–349.
- [25] James C Bouwer et al. "Deceleration of probe beam by stage bias potential improves resolution of serial block-face scanning electron microscopic images". *Advanced structural and chemical imaging* 2.1 (2016), pp. 1–13.
- [26] Ryan Lane et al. "Optimization of negative stage bias potential for faster imaging in large-scale electron microscopy". *Journal of structural biology: X* 5 (2021), p. 100046.
- [27] Martijn T Haring et al. "Automated sub-5 nm image registration in integrated correlative fluorescence and electron microscopy using cathodoluminescence pointers". *Scientific reports* 7.1 (2017), pp. 1–9.

- [28] Pascal de Boer et al. “Large-scale electron microscopy database for human type 1 diabetes”. *Nature communications* 11.1 (2020), pp. 1–9.
- [29] Raimond BG Ravelli et al. “Destruction of tissue, cells and organelles in type 1 diabetic rats presented at macromolecular resolution”. *Scientific reports* 3.1 (2013), pp. 1–6.
- [30] AC Zonnevylle et al. “Integration of a high-NA light microscope in a scanning electron microscope”. *Journal of microscopy* 252.1 (2013), pp. 58–70.
- [31] Yoram Vos et al. “Retarding field integrated fluorescence and electron microscope”. *Microscopy and Microanalysis* 27.1 (2021), pp. 109–120.
- [32] David G Lowe. “Object recognition from local scale-invariant features”. *Proceedings of the seventh IEEE international conference on computer vision*. Vol. 2. Ieee. 1999, pp. 1150–1157.
- [33] Stephan Saalfeld et al. “CATMAID: collaborative annotation toolkit for massive amounts of image data”. *Bioinformatics* 25.15 (2009), pp. 1984–1986.
- [34] Johannes Schindelin et al. “Fiji: an open-source platform for biological-image analysis”. *Nature methods* 9.7 (2012), pp. 676–682.
- [35] Stephan Saalfeld et al. “Elastic volume reconstruction from series of ultrathin microscopy sections”. *Nature methods* 9.7 (2012), pp. 717–720.
- [36] Khaled Khairy, Gennady Denisov, and Stephan Saalfeld. “Joint deformable registration of large EM image volumes: a matrix solver approach”. *arXiv preprint arXiv:1804.10019* (2018).
- [37] Perrine Paul-Gilloteaux et al. “eC-CLEM: flexible multidimensional registration software for correlative microscopies”. *Nature methods* 14.2 (2017), pp. 102–103.
- [38] Christian Franke et al. “Correlative single-molecule localization microscopy and electron tomography reveals endosome nanoscale domains”. *Traffic* 20.8 (2019), pp. 601–617.
- [39] Maarten W Tuijtel et al. “Correlative cryo super-resolution light and electron microscopy on mammalian cells using fluorescent proteins”. *Scientific reports* 9.1 (2019), pp. 1–11.
- [40] Chia-Wei Lee et al. “Selective autophagy degrades nuclear pore complexes”. *Nature cell biology* 22.2 (2020), pp. 159–166.
- [41] Shigeki Watanabe et al. “Protein localization in electron micrographs using fluorescence nanoscopy”. *Nature methods* 8.1 (2011), pp. 80–84.
- [42] Maria G Paez-Segala et al. “Fixation-resistant photoactivatable fluorescent proteins for CLEM”. *Nature methods* 12.3 (2015), pp. 215–218.
- [43] Wanda Kukulski et al. “Correlated fluorescence and 3D electron microscopy with high sensitivity and spatial precision”. *Journal of Cell Biology* 192.1 (2011), pp. 111–119.

- [44] Christopher J Peddie et al. “Correlative and integrated light and electron microscopy of in-resin GFP fluorescence, used to localise diacylglycerol in mammalian cells”. *Ultramicroscopy* 143 (2014), pp. 3–14.
- [45] Zhifei Fu et al. “mEosEM withstands osmium staining and Epon embedding for super-resolution CLEM”. *Nature methods* 17.1 (2020), pp. 55–58.
- [46] Nils Eckstein et al. “Microtubule Tracking in Electron Microscopy Volumes”. *International Conference on Medical Image Computing and Computer-Assisted Intervention*. Springer. 2020, pp. 99–108.
- [47] Jing Liu et al. “Automatic reconstruction of mitochondria and endoplasmic reticulum in electron microscopy volumes by deep learning”. *Frontiers in neuroscience* 14 (2020), p. 599.
- [48] Larissa Heinrich et al. “Whole-cell organelle segmentation in volume electron microscopy”. *Nature* 599.7883 (2021), pp. 141–146.
- [49] Chawin Ounkomol et al. “Label-free prediction of three-dimensional fluorescence images from transmitted-light microscopy”. *Nature methods* 15.11 (2018), pp. 917–920.
- [50] Rick Seifert et al. “DeepCLEM: automated registration for correlative light and electron microscopy using deep learning”. *F1000Research* 9.1275 (2020), p. 1275.
- [51] Julia Buhmann et al. “Automatic detection of synaptic partners in a whole-brain *Drosophila* electron microscopy data set”. *Nature Methods* 18.7 (2021), pp. 771–774.
- [52] AA Wanner, MA Kirschmann, and C Genoud. “Challenges of microtome-based serial block-face scanning electron microscopy in neuroscience”. *Journal of microscopy* 259.2 (2015), pp. 137–142.
- [53] Kenneth J Hayworth et al. “Imaging ATUM ultrathin section libraries with WaferMapper: a multi-scale approach to EM reconstruction of neural circuits”. *Frontiers in neural circuits* 8 (2014), p. 68.
- [54] Thomas Templier. “MagC, magnetic collection of ultrathin sections for volumetric correlative light and electron microscopy”. *Elife* 8 (2019), e45696.